Hole drift velocity in silicon*

G. Ottaviani, L. Reggiani, C. Canali, F. Nava, and A. Alberigi-Quaranta
Istituto di Fisica dell'Università, Via Università 4, Modena, Italy
(Received 16 October 1974; revised manuscript received 20 May 1975)

Drift velocities for holes in high-purity Si were measured for fields between about 3 and 5×10^4 V/cm and temperatures between 6 and 300°K for the crystallographic directions ⟨100⟩, ⟨110⟩, and ⟨111⟩. The Ohmic mobility is theoretically interpreted on the basis of a two-band model consisting of a spherical parabolic and a spherical nonparabolic band, and the relaxation-time approximation. The low-temperature Ohmic mobility is strongly influenced by the nonparabolicity of the heavy-hole band. The high-field region ($E\geq 10^3$ V/cm) was analyzed using a single warped heavy-hole band model and a Monte Carlo technique. Anisotropy of hot-hole drift velocity is associated with warping of the valence band. Optical- and acoustic-scattering mechanisms are found to be of comparable strength.

I. INTRODUCTION

This is the second of two papers (see Ref. 1, hereafter called I), which present experimental and theoretical investigation of the transport properties of electrons and holes in Si. This element has been studied intensively for several decades, yet hole transport in this material is far from being understood in terms of a microscopic model.

The purpose of this paper is to describe a detailed analysis of transport properties of holes in Si in accordance with experimental and theoretical findings. New measurements of hole-drift velocity were performed in the temperature range 6–77 °K and for electric fields between 3 and 10^4 V/cm applied parallel to the crystallographic directions ⟨100⟩, ⟨110⟩, and ⟨111⟩; these results complete a previous experimental investigation carried out between 77 and 300 °K.[2]

The theoretical analysis takes into account the whole range of temperatures, having as its main objective the quantitative correlation between experimental results and some peculiarities of the hole energy spectrum, namely, double degeneracy, nonparabolicity, and warping.

To overcome difficulties in theoretical calculations the Si valence band was approximated by two models: (a) the two-band model consisting of a spherical, parabolic and a spherical, nonparabolic band; (b) the one-band, warped and parabolic, model. Model (a) was used together with the relaxation-time approximation for the theoretical interpretation of Ohmic mobility. Model (b) was used following a Monte Carlo technique for the study of the anisotropy of hot-hole drift velocity.

In the interests of consistency the same deformation-potential parameters were used and a strict correlation between the band models and the Si valence band (deduced from cyclotron resonance experiments and $\vec{k}\cdot\vec{p}$ band-structure calculations) was maintained. Furthermore, discrepancies arising out of the different approximations were estimated.

Section II presents experimental data relating to hole-drift velocity. Section III describes the theoretical approach, presenting different band models and scattering mechanisms. In Sec. IV the theoretical and experimental results are compared and discussed.

II. EXPERIMENTAL TECHNIQUE AND RESULTS

The experimental data relating to hole-drift velocity were obtained using the time-of-flight technique. The characteristics and the limitations of this technique have been widely discussed in other papers[2–6] and were reviewed in I.

The measurements reported in the present paper were made on the purest available Si. It is worth pointing out that the same samples were used to measure the drift velocity of both holes and electrons, the only difference being that the impinging radiation (30-keV electrons) was sent to opposite contacts.

According to the analysis in I, the thermalization process of the highly excited carriers produced by the impinging radiation is, under our experimental conditions, much faster than transit time across the sample, since the drift velocities measured are always independent of sample thickness.

Assuming the electric field inside the sample to be nearly constant, the main sources of errors affecting the drift-velocity data are in the measurements of sample thickness, transit time, and applied voltage. The total experimental error of the drift velocity of holes is less than ±5%. Furthermore, owing to signal-to-noise ratio, the lowest value obtained with our apparatus for the measured v_d is about 10^6 cm/sec.

Experimental results relating to hole-drift velocity for temperatures between 6 and 300 °K and electric fields ranging between 3 and 10^4 V/cm applied in the ⟨100⟩ and ⟨111⟩ directions are shown in Fig. 1. For clarity, the data are reported as solid lines, each line representing the average value of more than 200 determinations of

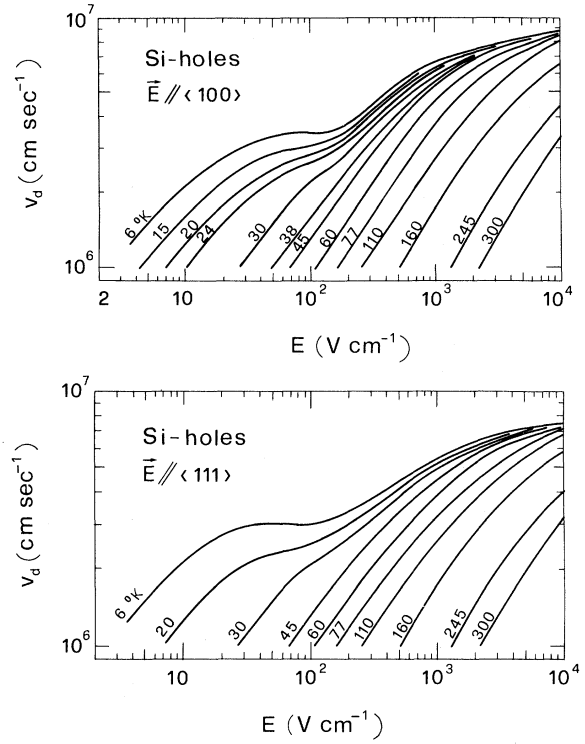

FIG. 1. Hole drift velocity v_d as a function of the electric field E applied parallel to the ⟨100⟩ and ⟨111⟩ crystallographic axes at several temperatures. The data above 77 °K are partially reported from Ref. 2.

drift velocity performed in different samples.

Some of the data obtained with the same experimental technique in the range 77–300 °K and published in a previous paper[2] are also included. In order to show the anisotropic effects more clearly, the data obtained by applying the field parallel to the ⟨100⟩, ⟨111⟩, and ⟨110⟩ directions at temperatures of 6, 77, and 300 °K are directly compared in Fig. 2.

The main features of the present data can be summarized as follows:

(a) For $T > 100$ °K, the Ohmic region is reached (see Fig. 1). For $T < 100$ °K, even at the lowest electric field the drift velocity is not proportional to the electric field, indicating that the Ohmic condition is not reached. Nevertheless, at the lowest electric field the curves of v_d for different crystallographic directions combine. At 6 °K, a mobility as high as 3.5×10^5 cm^2/V was obtained at $E = 3$ V/cm.

(b) The hole-drift velocity exhibits an anisotropic behavior with higher values for v_d in the ⟨100⟩ than in the ⟨111⟩ direction, and with the lowest value in the ⟨110⟩ direction. This anisotropy is best evidenced by lowering the temperature, its maximum effect (v_d values in the ⟨100⟩ direction 20% and 30% greater, respectively, than those in the ⟨111⟩ and ⟨110⟩ directions) being observed at 6 °K. At the highest fields (about 10^4 V/cm) the anisotropy appears to saturate.

(c) A net defined saturation region of v_d for the three different directions shows up in a narrow range of fields between 50 and 150 V/cm at 6 °K. This effect gradually disappears as temperature is increased until, at temperatures above about 38 °K, it is no longer apparent.

Comparison of our data with other available data in the literature is very difficult owing to the scarcity of published results. In particular, to the authors' knowledge, no other experiments on drift velocity as a function of electric field have been reported below 300 °K, other authors restricting their studies to the measurement of Ohmic mobility as a function of temperature.

A. Ohmic mobility and comparison with other data

As reported above, the present data do not reach the linear-response region (Ohmic mobility) for temperatures lower than 100 °K. In order to estimate how Ohmic mobility is approached, we have collected in Fig. 3 a family of curves reporting the

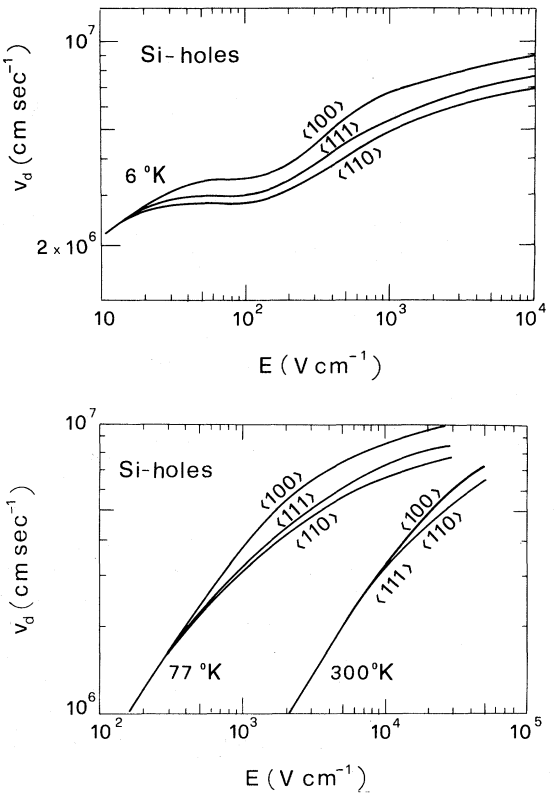

FIG. 2. Hole drift velocity as a function of the electric field E applied parallel to the ⟨100⟩, ⟨111⟩, and ⟨110⟩ crystallographic axes at $T = 6$, 77, and 300 °K.

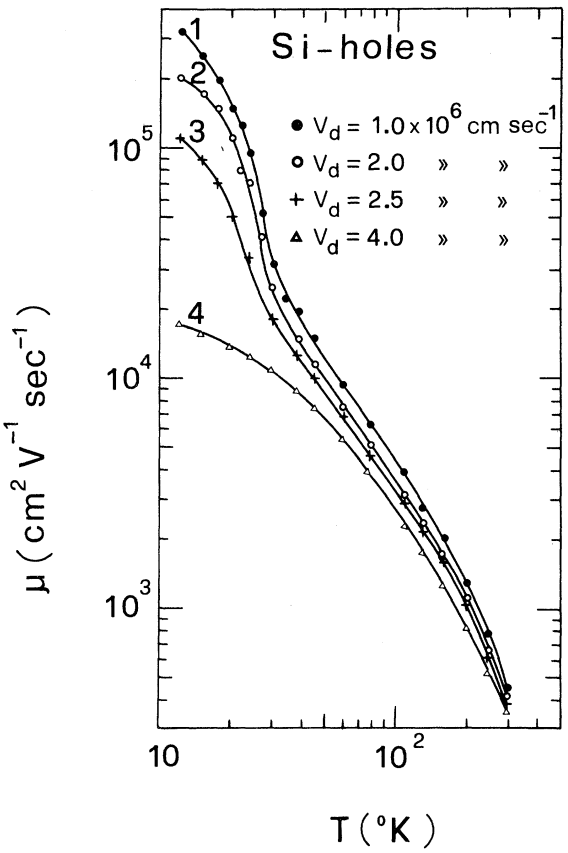

FIG. 3. Temperature dependence of the mobility μ obtained by the ratio v_d/E of Fig. 1 for holes in Si. Curves 1–4 refer to fixed values of the drift velocities ranging from 1×10^5 to 4×10^6 cm/sec.

ratio v_d/E as a function of temperature. This ratio was obtained from the data shown in Fig. 1 at a fixed v_d value. Accordingly, curve 1 refers to $v_d = 1\times10^6$ cm/sec and curves 2, 3, and 4 refer to v_d values of 2×10^6, 2.5×10^6, and 4×10^6 cm/sec, respectively. Since drift velocity in the linear-response region should be negligible with respect to thermal-equilibrium velocity, progressive lowering of the chosen v_d value causes the different curves of Fig. 3 to come closer and closer to the Ohmic mobility limit, which is most nearly represented by curve 1. As may be expected, the curve 1 becomes more and more approximate as the temperature is lowered, therefore the value of $v_d = 10^6$ cm/sec becomes more and more comparable with the thermal-equilibrium velocity. Thus, the present results may be said to systematically underestimate Ohmic mobility at the lower temperatures.

The μ obtained from the lowest v_d value exhibits a sudden increase at temperatures below about 40 °K, thus leading one to suspect an anomalous behavior of the lattice-controlled Ohmic mobility.[7]

In Fig. 4(a) the experimental data of Ohmic mobility obtained by several authors[8–11] with ionized impurity concentrations ranging between 10^{12} and

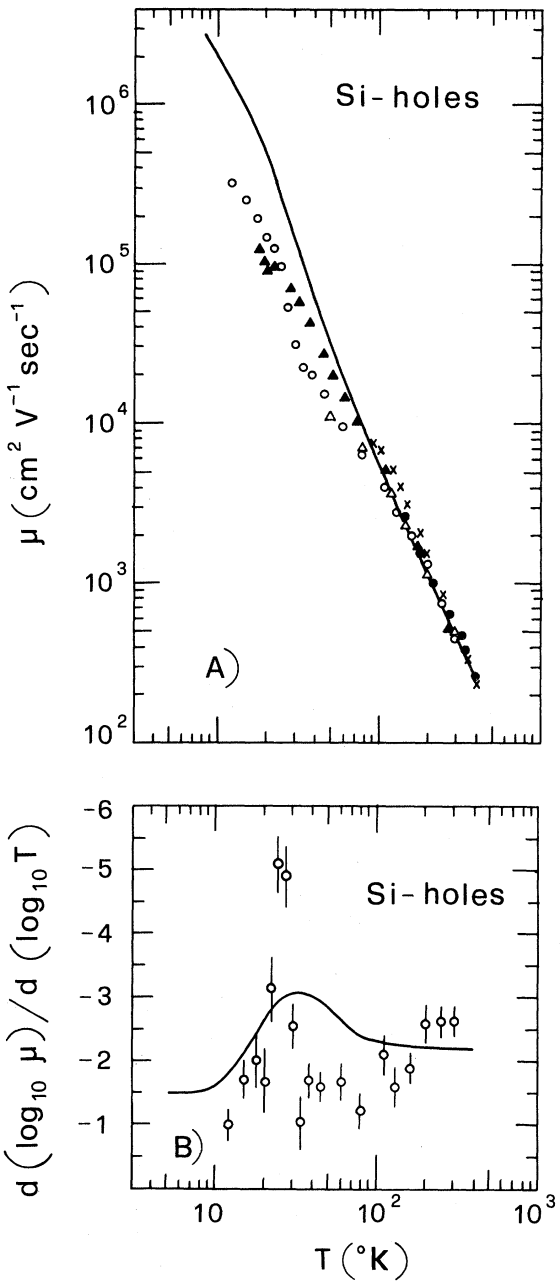

FIG. 4. (a) Mobility μ of holes in Si as a function of temperature. The continuous line shows the theoretical results. ○—present data (see curve 1 of Fig. 3). ▲—experimental values of the drift mobility deduced from Fig. 1 of Ref. 8. ×—experimental values of the drift mobility of minority carriers deduced from Fig. 4 of Ref. 9. △—experimental data of Hall mobility deduced from Fig. 10 (sample 1053, p type) of Ref. 10. ●—experimental values of the conductivity mobility deduced from Fig. 12 of Ref. 11. (b) Temperature dependence of $d\log_{10}\mu/d\log_{10}T$. The continuous line refers to theoretical results. ○—present data.

10^{14} cm^{-3} are reported as a function of temperature, together with the experimental results of curve 1 of Fig. 3. Moreover, also reported in Fig. 4(a) are the theoretical results that will be discussed in Sec. IV.

In the region of temperatures above about 100 °K, different experimental data agree as to the absolute value of μ and to its temperature dependence, thus strongly supporting the hypothesis of a lattice-controlled mobility. Below about 100 °K, however, data are open to interpretation. In the region of low temperatures, Logan *et al.*,[8] through conductivity and Hall-effect measurements, found μ proportional to T^{-2}. Our data, obtained from purer samples with a different technique show a sharp increase of mobility below about 40 °K (see Fig. 3). In order to quantitatively estimate this effect we have reported in Fig. 4(b) the $d\log_{10}\mu/d\log_{10}T$ as a function of T. Also reported in the same figure is the theoretical result discussed in Sec. IV. It is seen here that a peak in the $d\log_{10}\mu/d\log_{10}T$ as high as -5 has been evidenced by experiments in the temperature range 20–30 °K.

III. THEORY

The aim of this section is to develop a microscopic interpretation of hole-drift velocity following a semiclassical approach. The Boltzmann-equation model involves the scattering mechanisms and the valence-band structure.

A. Scattering mechanisms

The lattice-scattering mechanisms in Si are due predominantly to nonpolar-optical and acoustic phonons.[12,13] Owing to the particular form of the Si valence band, one must take into account intraband as well as interband transitions. Both acoustic and optical phonons are permitted by symmetry arguments within and between the two $\vec{k}=0$ degenerate valence bands.[14,15] Furthermore, the characteristic p-like symmetry of the hole wave functions permits acoustic-transverse phonons to be effective in scattering.[14]

In the present paper the spin-orbit band will be ignored, this approximation being well justified as discussed in Sec. III B. Furthermore, we shall not consider other scattering mechanisms arising from defects (e.g., ionized and neutral impurity, and dislocations) owing to the high purity and perfection of the crystals used in experiments (see Tables I and II of Paper I).

The theoretical scattering cross section for the interaction between holes and phonons has been widely treated in the literature in the case of covalent semiconductors.[14,16–20] The original expressions for the transition rate are, however, quite complicated and introduce considerable difficulties into analytical calculation. Thus, a simplified expression which, within the deformation-potential approach, accounts for the p-like symmetry of hole wave functions is used.[21–24] Accordingly, the scattering probability per unit time and N processes, P_i^f, between initial $\vec{k}$ and final $\vec{k}'$ states with energy ϵ_i and ϵ_f, for acoustic- and optical-scattering mechanisms is, respectively:

$$P_i^f(\vec{k},\vec{k}') = \frac{2\pi}{\hbar} B_{\mathrm{ac,op}} G(\nu)\delta(\epsilon_f - \epsilon_i)\ , \tag{1}$$

with

$$B_{\mathrm{ac}} = \frac{\hbar E_1^{0^2}}{2V\rho s}\left|\vec{k}-\vec{k}'\right|\left(N_q+\tfrac{1}{2}\pm\tfrac{1}{2}\right)\ , \tag{2}$$

$$B_{\mathrm{op}} = \frac{\hbar^2 (D_t K)^2}{2V\rho K_B \theta_{\mathrm{op}}}\left(N_q+\tfrac{1}{2}\pm\tfrac{1}{2}\right)\ , \tag{3}$$

$$G(\nu) = \begin{cases} \frac{1}{4}(1+3\cos^2\nu)\ , & \text{intraband transitions} \\ \frac{3}{4}\sin^2\nu\ , & \text{interband transitions}\ . \end{cases} \tag{4}$$

ν being the scattering angle, V the crystal volume, ρ the crystal density, $s=\frac{1}{3}s_l+\frac{2}{3}s_t$ the weight average of the longitudinal, s_l, and transverse, s_t, sound velocity; θ_{op} is the optical-phonon energy, assumed $\vec{q}$ independent; N_q is the Bose-Einstein distribution function; E_1^0 and D_tK are the deformation-potential parameters for acoustic and optical scattering, respectively. The ± signs in Eqs. (2) and (3) refer to emission and absorption processes.

Bulk constants and deformation-potential parameters are reported in Table I. The acoustic-scattering mechanism has been considered, as usual, in the elastic approximation, and the effectiveness of the transverse as well as longitudinal acoustic

TABLE I. Constants of Si used for calculations.

Quantity	Value	Unit	References
ρ	2.329	g/cm^3	25
θ_{op}	735	°K	26
s_l	9.04×10^5	cm/sec	27
s_t	5.34×10^5	cm/sec	27
$\lvert A\rvert$	4.27	•••	28
$\lvert B\rvert$	0.63 ± 0.08	•••	28
$\lvert N\rvert$ [a]	8.75 ± 0.25	•••	28
Δ	0.044	eV	29
m_{10}/m_0	0.55	•••	7
m_{11}/m_0	1.7	•••	pw[b]
m_2/m_0	0.2	•••	7
β	0.69	•••	pw
ϵ_0/K_B	70	°K	7
ϵ_1/K_B	130	°K	7
E_1^0	2.2	eV	pw
D_tK	5×10^8	eV/cm	pw

[a] $C^2=\frac{1}{3}(N^2-9B^2)$. [b] pw, present work.

modes has been conveyed in the deformation-potential parameter.

B. Si valence band

In this section we briefly review the Si-valence-band structure and present two approximated models used for the interpretation of experimental results.

The hole spectrum in Si consists of three bands,[30,31] two degenerate at $\vec{k}=0$, usually called heavy- and light-mass band, and a third one split at $\vec{k}=0$ by Δ, Δ being the spin-orbit energy. The theoretical analysis of Kane[31] gives the energy wave vector relationship for each band in terms of Δ and of the valence-band parameters A, B, and C by considering the first term of a perturbation expansion of the $\vec{k}\cdot\vec{p}$ and spin-orbit perturbations. For each band the surfaces of constant energy are not spherical, the band curvature being a function of direction $\vec{k}/k$, and in this sense the bands are warped. This effect is mainly because of the similarity of the Bloch wave functions of holes to atomic p functions.[32] Furthermore, owing to the spin-orbit interaction, the energy of each band varies nonparabolically with k. The effect of nonparabolicity, which is more pronounced in the $\langle 110\rangle$ direction, is mostly effective at energies near $\frac{1}{3}\Delta$. In the limits of $\epsilon/\Delta \ll 1$ and $\epsilon/\Delta \gg 1$ all bands are parabolic.[31]

The degree of warping of the heavy and light bands, as calculated from Eq. (30) of Ref. 31, is illustrated in Figs. 5(a) and 5(b) at two energy values (i.e., $\epsilon/\Delta=0.02$ and $\epsilon/\Delta=5$).

In Fig. 5(a) curves 1, 2, and 3 reproduce the experimental uncertainties of the valence-band parameters B and C (see Table I), to which the heavy band is more sensitive in the high-energy region.

To estimate the nonparabolicity effect, the equilibrium carrier concentration for each band was calculated under the condition of nondegenerate statistics. Then, by equating the results so obtained to those of a free-electron band model a temperature-dependent isotropic effective mass m_i is defined,

$$\left(\frac{m_i}{m_0}\right)^{3/2} = \pi^{-3/2}\int \exp\left(\frac{\epsilon_i(\vec{x})}{K_B T}\right) d^3x \,, \qquad (5)$$

with

$$x=\hbar k/(2m_0 K_B T)^{1/2} \,; \quad i=h,\, l,\, so \,.$$

m_0 is the free-electron mass, ϵ_i is the solution of Kane's cubic equation,[31] and h, l, and so stand for heavy, light, and spin-orbit bands, respectively. In Fig. 6(a) the effective masses for the heavy band, m_h/m_0, and light band, m_l/m_0, at equilibrium are plotted as a function of temperature. In Fig. 6(b) the density-of-states ratios of light to heavy band, $n_l/n_h=(m_l/m_h)^{3/2}$, and of spin orbit to heavy band, $n_{so}/n_h=(m_{so}/m_h)^{3/2}e^{-\Delta/K_B T}$ at equilibrium are shown as a function of temperature. The shaded region of Figs. 6(a) and 6(b) show uncertainty regarding the quantities considered owing to the spread of the valence-band parameters B and C, while the continuous lines refer to the two-band approximation described below. For the heavy band [Fig. 6(a)] the pair $B=-0.55$ and $C=-5.11$ was found to exhibit the maximum nonparabolic effect with $m_h(T=1500\ ^\circ\mathrm{K})/m_h(T=0\ ^\circ\mathrm{K})=4.53$, curve 1, while pair $B=-0.71$ and $C=-4.75$ exhibits the minimum effect with $m_h(T=1500\ ^\circ\mathrm{K})/m_h(T=0\ ^\circ\mathrm{K})=1.89$, curve 2. The ambiguity for the heavy-hole effective mass is reflected in the density-of-states ratios reported in Fig. 6(b). For the range of temperatures up to 300 °K the calculated values of n_l/n_h are within 0.15

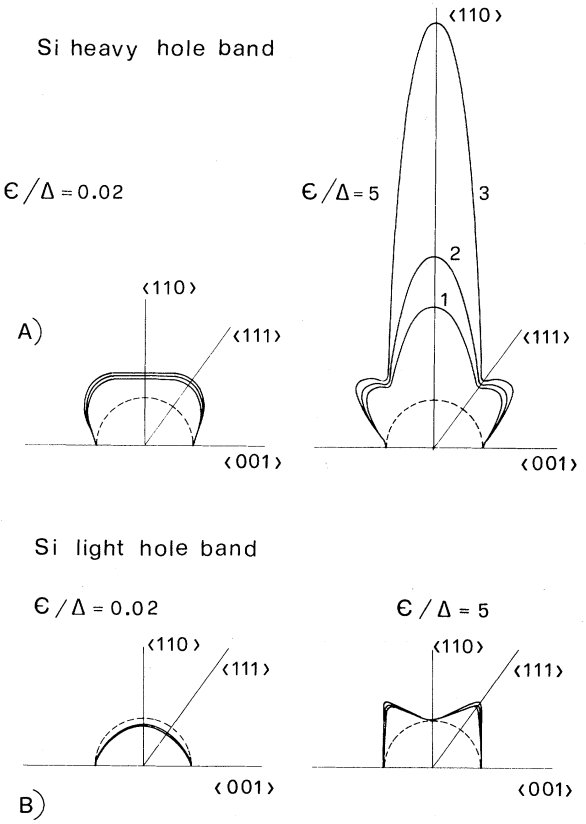

FIG. 5. (a) energy contour in the (110) plane of the Si heavy-hole band for two values of the energy: $\epsilon/\Delta=0.02$ and $\epsilon/\Delta=5$. Different curves reproduce experimental uncertainties on B and C. For the case $\epsilon/\Delta=5$, curve 1 refers to $A=-4.27$, $B=-0.71$, and $C=4.75$; curve 2 refers to $A=-4.27$, $B=-0.63$, and $C=4.93$; curve 3 refers to $A=-4.27$, $B=-0.55$, and $C=5.11$. For the case $\epsilon/\Delta=0.02$ the uncertainties on B and C yield negligible effects. The inner dashed circle represents a spherical band. (b) The same as in (a) for the Si light-hole band. The uncertainties on B and C yield negligible effects for both cases.

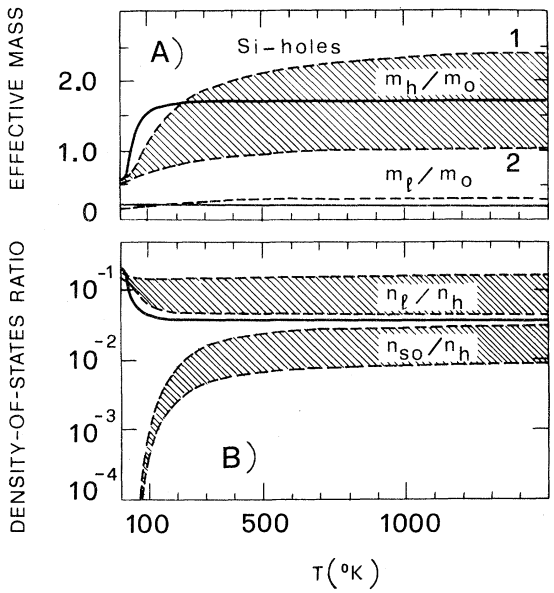

FIG. 6. (a) Equilibrium density-of-states effective mass for the heavy band, m_h/m_b, and light band, m_l/m_0, as a function of temperature. The shaded region between dashed curves refers to the uncertainties of the valence-band parameters. Dashed curve 1 refers to $A=-4.27$, $B=-0.55$, and $C=5.11$; dashed curve 2 refers to $A=-4.27$, $B=-0.71$ and $C=4.75$. The continuous line refers to the two-band model used in Sec. III B. (b) Equilibrium density-of-states ratio of light to heavy band, n_l/m_h, and splitoff to heavy band, n_{so}/n_n as a function of temperature. The shaded region between dashed curves refers to uncertainties of the valence-band parameters. The continuous line refers to the two-band model used in Sec. III. B.

and 0.05 and n_{so}/n_h is always lower than 0.02. The small value of n_{so}/n_h found, and a scattering time dominated by interband processes, and thus comparable with that of the heavy band, justify the omission of the spin-orbit band in present calculations.

1. Two-band model

This model consists of a spherical nonparabolic heavy band and a spherical parabolic light band[7] which, assuming positive energies for holes, is defined by:

$$\epsilon_{v1}=\begin{cases}\hbar^2k^2/2m_{10} & \text{for } 0\leq\epsilon_{v1}\leq\epsilon_0\\ \hbar k/(2m_{10}\alpha)^{1/2}+\epsilon_\alpha & \text{for } \epsilon_0<\epsilon_{v1}\leq\epsilon_1,\\ \hbar^2k^2/2m_{11} & \text{for } \epsilon_1<\epsilon_{v1}\end{cases} \tag{6}$$

$$\epsilon_{v2}=\hbar^2k^2/2m_2\,,$$

$$\alpha=\left(\frac{(\epsilon_1 m_{11}/m_{10})^{1/2}-\epsilon_0^{1/2}}{\epsilon_1-\epsilon_0}\right)^2;\quad \epsilon_\alpha=\epsilon_0-(\epsilon_0/\alpha)^{1/2}\,. \tag{7}$$

The subscripts 1 and 2 stand for heavy and light bands, respectively. m_{10} and m_{11} fix the effective mass of the heavy band at the bottom, $\epsilon_{v1}=0$, and at energies $\epsilon_{v1}\geq\epsilon_1$, respectively; ϵ_0 and ϵ_1 define the $\vec{k}$-linear region of the spectrum which joins the two parabolic regions of the heavy band; m_2 fixes the effective mass of the light band, which is assumed to be parabolic.

The values for these parameters (see Table I), except for m_{11}, have been taken from Ref. 7; $m_{11}=1.7m_0$ is an average within the experimental uncertainty of B and C.

To check the reliability of this band model, in Figs. 6(a) and 6(b) the effective masses m_h/m_0 and m_l/m_0 and the density-of-states ratio n_l/n_h calculated from Eqs. (6) and (7) are represented by a continuous line. From this figure it is seen that, for temperatures up to 200 °K, the present model slightly overestimates the nonparabolicity effect with respect to band-structure calculations. However, as a first approximation it would appear to account satisfactorily for the large nonparabolicity of the heavy-band mass.

2. One-band model

This model consists of a warped and parabolic heavy band which, assuming positive energies for holes, is defined by

$$\epsilon_v=(1-\beta)ak^2\{1-[b^2+c^2(\sin^4\vartheta\cos^2\varphi\sin^2\varphi+\sin^2\vartheta\cos^2\vartheta)]^{1/2}\}, \tag{8}$$

$$a=\frac{\hbar^2|A|}{2m_0};\quad b=\frac{|B|}{|A|};\quad c=\frac{|C|}{|A|}$$

with a warping factor η between the $\langle100\rangle$ and $\langle111\rangle$ $\vec{k}$ directions,

$$\eta\equiv\frac{k_{100}}{k_{111}}=\left(\frac{1-(b^2+\frac{1}{3}c^2)^{1/2}}{1-b}\right)^{1/2}.$$

β is a numerical parameter, which enables us either to change the warping, keeping the same value for the density-of-states effective mass, or to change the value of the density-of-states effective mass, preserving the warping. In this way, it will be of use in the study of the effect of warping alone on mobility and hot-hole drift velocity and in estimating the effect of nonparabolicity on v_d at high fields as will be discussed in Sec. IV B.

The warping exhibited by Eq. (8) with the values of A, B, and C reported in Table I is shown in Fig. 5(a) under $\epsilon/\Delta=0.02$. The values $\beta=0$ and $\beta=0.69$ reproduce a density-of-states effective mass $m_h(\beta=0)=0.53m_0$ and $m_h(\beta=0.69)=1.7m_0$, which are consistent with the $\epsilon_{v1}<\epsilon_0$ and $\epsilon_{v1}>\epsilon_1$ limiting conditions of the two-band model.

C. Solution of the Boltzmann equation

In this section two different approaches are used to solve the Boltzmann equation: the relaxation time approximation and the Monte Carlo technique. Since the first approach is confined to the interpretation of the linear-response region, and the second has been proved to lead to a distribution function which satisfies the Boltzmann equation,[33] the transport approach, within the limitations of the present models, is treated rigorously.

1. Relaxation-time approximation for Ohmic mobility

In the two-band model the total mobility μ is

$$\mu = \frac{\mu_1 + (n_2/n_1)\mu_2}{1 + n_2/n_1} \tag{9}$$

with n_2/n_1 the ratio of carrier concentration between light and heavy bands at equilibrium, and μ_i $(i=1, 2)$ the mobility of each band which in the relaxation-time approximation is given by,

$$\mu_i = \frac{e}{\hbar^2}\int \left|\nabla_{k_x}\epsilon\right|_i^2 \tau_i(\epsilon)\frac{\partial f_{0i}}{\partial \epsilon} d^3k \,, \tag{10}$$

where τ is the relaxation time and f_0 the Boltzmann distribution function at equilibrium normalized to unity.

τ was calculated including acoustic and optical scattering for the two-band model defined by Eqs. (6) and (7).[34] Acoustic modes have been treated in the energy equipartition approximation and for optical modes the heavy-band spectrum has been approximated with its high-energy expression (i.e., $\epsilon_{v1} = \hbar^2k^2/2m_{11}$) in the whole range of energy. Accordingly, by considering interband as well as intraband scattering both types of carriers are found to have the same relaxation time defined by,

$$\tau^{-1} = \frac{m_{10}^{3/2}K_BTE_1^{0^2}}{2^{1/2}\pi\hbar^4\rho s^2}\epsilon^{1/2}\left\{\left[\mathcal{L}(\epsilon) + \left(\frac{m_2}{m_{10}}\right)^{3/2}\right] + \frac{1}{2}\left(\frac{\omega_{op}}{\omega_{ac}}\right)^2\left(\frac{m_{11}}{m_{10}}\right)^{3/2}\frac{\theta_{op}}{T}\left[N_{op}(\epsilon + K_B\theta_{op})^{1/2} + (N_{op}+1)(\epsilon - K_B\theta_{op})^{1/2}\right]\left[1 + \left(\frac{m_2}{m_{11}}\right)^{3/2}\right]\right\} , \tag{11}$$

with

$$\mathcal{L}(\epsilon) = \begin{cases} 1 & \text{for } 0 \le \epsilon_{v1} \le \epsilon_0 \\ 2\alpha^{3/2}[(\epsilon - \epsilon_\alpha)/\epsilon^{1/2}] & \text{for } \epsilon_0 < \epsilon_{v1} \le \epsilon_1 \\ (m_{11}/m_{10})^{3/2} & \text{for } \epsilon_1 < \epsilon_{v1} \end{cases} , \tag{12}$$

and

$$\frac{\omega_{op}}{\omega_{ac}} = \frac{(D_tK)\hbar s}{E_1^0K_B\theta_{op}} ; \quad N_{op} = (e^{\theta_{op}/T} - 1)^{-1} .$$

In Eq. (11) the emission of an optical phonon can, of course, only occur for $\epsilon \ge K_B\theta_{op}$.

2. Monte Carlo technique

Following the time-average method, and assuming the time of scattering to be negligible with respect to free flight, for a carrier suffering a rate of momentum $\hbar\vec{k} = e\vec{E}$ the time-independent longitudinal v_d is[33]

$$v_d = \lim_{t\to\infty}\frac{1}{eEt}\sum(\epsilon_{v_f} - \epsilon_{v_i}) , \tag{13}$$

where the sum is evaluated over all carrier-free flights, starting from $t=0$. The sum in Eq. (13) was evaluated using a Monte Carlo technique as described in Ref. 33.

The angular dependence of the scattering probability per unit time and the integrated scattering probability were evaluated in accordance with Eqs. (1)–(4) making use of the one-band model reported in Eq. (8). Acoustic scattering in energy equipartition and in zero-point approximation, as well as optical-phonon scattering, were taken into account. The detailed calculations of the integrated scattering probabilities are reported in the Appendix. Each value of v_d at a given field was obtained as an average over several runs (from 5 to 10), thus reducing uncertainty to less than 5%.

IV. RESULTS AND DISCUSSION

The two main objectives of this section are: to analyze the lattice-controlled mobility as a function of temperature, taking into account the nonparabolicity of the heavy-mass band; and to correlate quantitatively the anisotropy of hot-hole v_d with the warping of the heavy valence band.

The analysis of Ohmic mobility by fixing the two deformation-potential parameters affords the basis for the interpretation of v_d at high fields. However, owing to the rough approximations introduced into the theory, a complete analysis of experiments outside the Ohmic region is beyond the scope of this paper. We have therefore confined our attention to the anisotropy of v_d, rather than to its absolute value. The results so obtained are by no means exhaustive but should form a guide for future refinements.

A. Ohmic mobility

Calculations make use of the relaxation time approximation and of the two-band model. The deformation-potential parameters E_1^0 and D_tK used

are reported in Table I.

The theoretical and experimental results for μ are compared in Fig. 4(a). Agreement is satisfactory in the temperature range 50–300 °K, while below 50 °K agreement is only qualitative. However, in the lowest temperature region, the data reported may not be claimed to exhibit a perfect lattice-controlled μ. The possible influence of impurity scattering in the data of Ref. 8 and the slight field dependence of the mobility in the present data both lead one to expect a mobility lower than in the case of pure lattice. Consequently, the theoretical results obtained in this temperature range would appear to offer a suitable basis for further investigations.

The results for the $d\log_{10}\mu/d\log_{10}T$ as a function of temperature reported in Fig. 4(b) afford a more direct check of the nonparabolicity influence on mobility through the resolution in temperature of the peak exhibited by $d\log_{10}\mu/d\log_{10}T$. The fact that the theoretical peak is broader than the experimental peak may be largely ascribable to the slight field dependence of the experimental μ below 100 °K; better agreement between the two peak values may be obtained if the warping of the valence band is explicity taken into account.

The present results show that light holes contribute appreciably to the total mobility, their contribution exceeding 25% over the whole range of temperatures, with a peak of 50% at 30 °K. This relevant importance of light holes in Si transport processes may largely be ascribed to the strong nonparabolicity of the heavy band.

The $\omega_{op}/\omega_{ac}=1.55$ obtained here assigns a slight prevalence of optical-scattering mechanisms over acoustic. In order to gain a clear understanding of the model used and of its limitations, theoretical curves calculated for different approximated models are reported in Fig. 7 in comparison with the curve of Fig. 4(a) (curve 1 of Fig. 7).

Curve 2, calculated taking only acoustic scattering into account, shows the relative importance of this scattering mechanism at different temperatures. At 400 °K acoustic and optical modes are seen to be of the same order of importance.

Curve 3 was calculated using the low-energy parabolic approximation for the heavy band ($\epsilon_{v1}=\hbar^2k^2/2m_{10}$ for $\epsilon_{v1}\geq 0$), and curve 4 was calculated using the high-energy parabolic approximation for the heavy band ($\epsilon_{v1}=\hbar^2k^2/2m_{11}$ for $\epsilon_{v1}\geq 0$). The constant ratio between the mobilities calculated for the two models at the same temperature is, in accordance with Ref. 35,

$$\frac{[1+(m_{10}/m_2)^{1/2}][1+(m_{11}/m_2)^{3/2}]^2}{[1+(m_{10}/m_2)^{3/2}]^2[1+(m_{11}/m_2)^{1/2}]}=14.56\ .$$

This value represents the maximum effect of nonparabolicity on mobility that can be expected using the present model.

Curve 5 was calculated using the heavy band only, as defined in Eq. (6), and the same constants as for curve 1. It systematically underestimates total mobility with respect to curve 1, the relative difference being 10% at 10 °K rising to 25% at 400 °K.

The following points should be noted. Warping effect has to be considered secondary in importance to those of nonparabolicity, as discussed in the next section. The omission of nonparabolicity in calculating the optical relaxation time should not have detectable effects. In fact, in the present model the nonparabolicity of the heavy band starts at $\epsilon_{v1}\leq 130$ °K, where optical scattering is found to be almost ineffective[36] owing to the high value of optical-phonon energy $\theta_{op}=735$ °K.

Present calculations should be limited to temperatures above about 8 °K, since below this temperature the ratio between acoustic-phonon energy in-

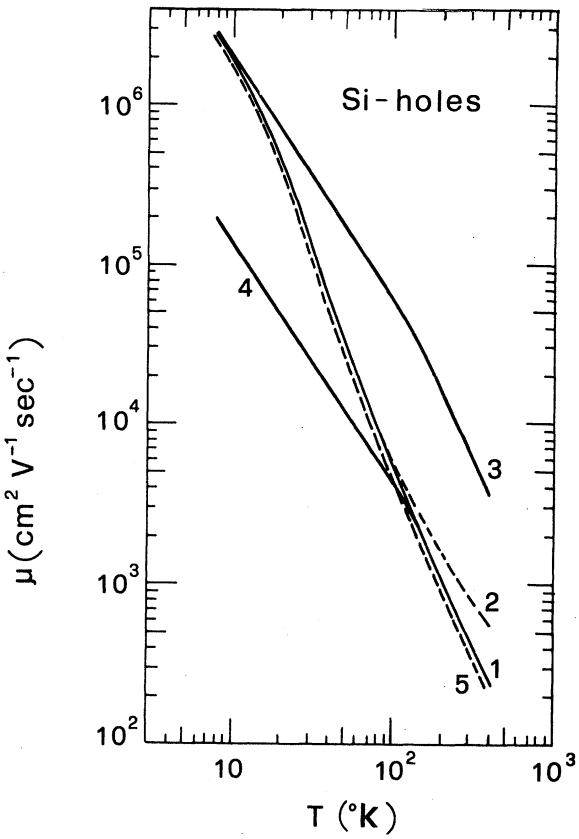

FIG. 7. Theoretical Ohmic mobility μ of holes in Si as a function of temperature for the different models used. Curve 1 is the same as reported in Fig. 4(a). Curve 2 accounts for acoustic scattering only. Curve 3 refers to the parabolic approximation for the heavy band (i.e., $\epsilon_{v1}=\hbar^2k^2/2m_{10}$ for $0\leq\epsilon_{v1}<\infty$). Curve 4 refers to the parabolic approximation for the heavy band (i.e., $\epsilon_{v1}=\hbar^2k^2/2m_{11}$ for $O\leq E_{v1}<\infty$). Curve 5 refers to the single nonparabolic-band approximation (heavy band).

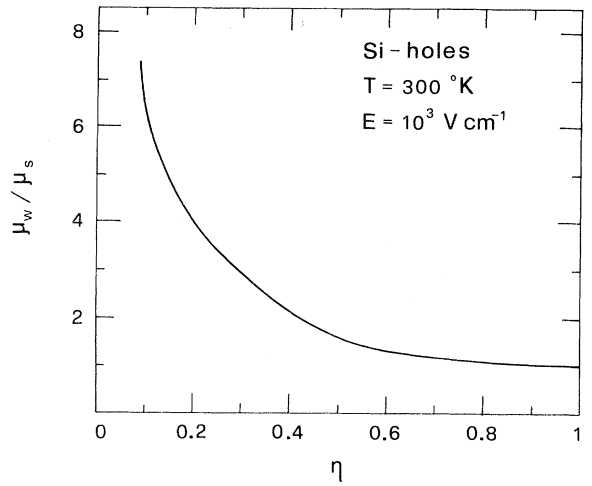

FIG. 8. Mobility for the warped case, μ_w, normalized to the value of the mobility for the spherical case, μ_s, as a function of the warped factor η. Calculations have been performed for $T=300\,°\mathrm{K}$, $E=10^3$ V/cm, and $m_h/m_0=1.7$.

volved in scattering and thermal energy is no longer negligible compared with unity, as required by the energy equipartition approximation.

B. High fields

The theoretical analysis of high-field experimental data $E \geq 10^3$ V/cm was performed using the results obtained in Monte Carlo technique and the one-band model. Before experimental and theoretical data are compared in detail, the model used is briefly discussed in connection with the following: (a) correlation between mobility and warping effects; (b) correlation between the anisotropy of hot-hole drift velocity and warping effects; (c) effect on anisotropy of the angular dependence of the scattering cross section.

(a) The correlation between warping and mobility was studied at $T=300\,°\mathrm{K}$ and $E=10^3$ V/cm where experiments are seen to be in the Ohmic region. Calculations where performed changing the warping factor η, assigning different values to the inverse valence-band parameter C and maintaining a fixed value of the density-of-states effective mass $m_h/m_0=1.7$ by means of appropriate values of β. The ratio μ_w/μ_s between the mobility for the warped case μ_w and the spherical case μ_s is reported in Fig. 8 as a function of η. Results show a monotonic decrease in μ_w/μ_s as warping decreases, the minimum value being obtained with a spherical band. This is owing to the fact that, in the warped case, the average conductivity effective mass, which determines mobility, is heavily weighted by small mass values. In Si, according to different $\vec{k}$ directions, the warping factor is found to range from 0.25 to 0.61 and the corresponding variation of μ_w/μ_s from Fig. 8 is from 1.3 to 3.4. These values should be taken as estimates of the warping effect only on mobility of holes in Si.

(b) The correlation between warping and anisotropy was studied at $T=77\,°\mathrm{K}$ and $E=10^4$ V/cm where experiments show the anisotropy of v_d. The anisotropic factor $(v_{d_{100}}/v_{d_{111}}-1)$ was calculated as a function of η by keeping the value of $m_h/m_0=1.7$ fixed. Results in Fig. 9 show a monotonic decrease of $(v_{d_{100}}/v_{d_{111}}-1)$ towards zero with η ranging between 0 and 1. This is because of the fact that when η reduces to zero, the effective mass in the $\langle 100\rangle$ direction also reduces to zero, thus leading to a strong enhancement of v_d in this direction.

(c) The effect on anisotropy of the angular dependence of the scattering cross section was investigated by comparing the results obtained for an angle-independent scattering probability $[G(\nu)=\frac{1}{2}]$ with those of an angle-dependent scattering probability, as given in Eq. (4). Calculations yield negligible differences between the two cases.

1. Comparison with experimental findings

Theoretical and experimental data of $v_{d_{100}}$ as a function of temperature are reported in Fig. 10(a) for $E=10^3$ V/cm and in Fig. 10(b) for $E=10^4$ V/cm. In order to estimate the effect introduced by the nonparabolicity of the heavy band, calculations were performed for two different values of the heavy mass: $m_h/m_0=0.53$ (dashed line) and $m_h/m_0=1.7$ (continuous line).

In the low-temperature region ($T<100\,°\mathrm{K}$) neither of the two values interprets experimental findings satisfactorily, even if both reflect the tendency of the data to remain constant despite temperature changes. In the high-temperature region ($T>100\,°\mathrm{K}$) calculations show an improvement of the agreement for the case of a heavy-hole effective mass $m_h/m_0=1.7$.

The nearly constant value assumed by theoretical

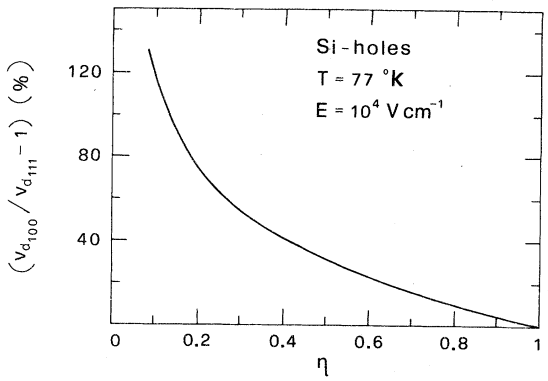

FIG. 9. Anisotropic factor $(v_{d_{100}}/v_{d_{111}}-1)$ as a function of the warped factor η. Calculations have been performed for $T=77\,°\mathrm{K}$, $E=10^4$ V/cm, and $m_h/m_0=1.7$.

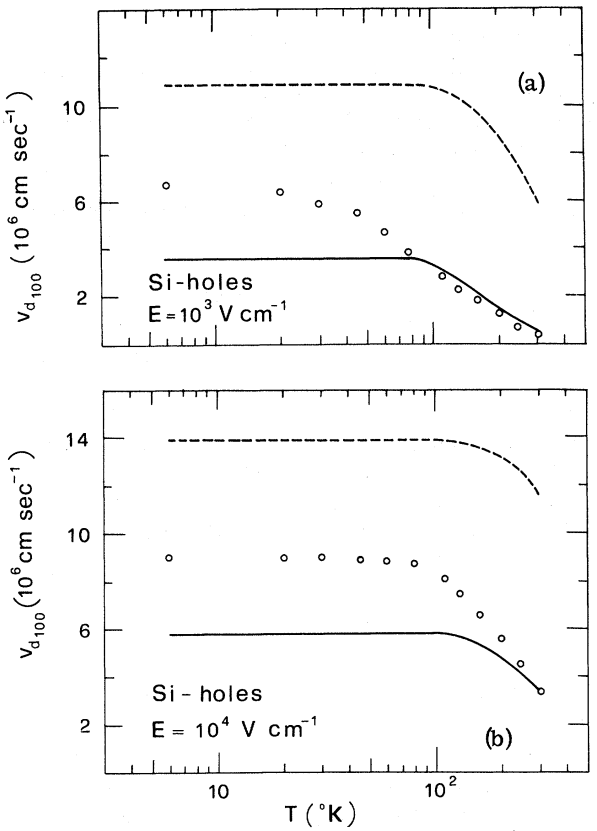

FIG. 10. (a) Drift velocity $v_{d_{100}}$ as a function of temperature in Si for an electric field $E=10^3$ V/cm. The dashed curve refers to the case $m_h/m_0=1.7$ (i.e., $\beta=0.69$) and the continuous line to the case $m_h/m_0=0.53$ (i.e., $\beta=0$). o—present data. (b) The same as in (a) for an electric field $E=10^4$ V/cm.

$v_{d_{100}}$ at T below about 100 °K is due to the prevalence of emission processes of optical phonons that result from the heating of holes by the field.

The disagreement between theoretical and experimental findings in the low-temperature region, which is more evident for the case of $E=10^4$ V/cm, is largely attributable to the over-crude approximation used for the heavy-band spectrum, particularly the omission of nonparabolicity. In fact, the contribution of the small effective-mass region should lead to an increase of the value of v_d with respect to the case of $m_h/m_0=1.7$. As an example, at 6 °K the theoretical results, with the heavy-hole effective mass corresponding to $m_h/m_0=0.53$ yield for $E=10^3$ V/cm a $v_{d_{100}}=1.08\times10^7$ cm/sec and for $E=10^4$ V/cm a $v_{d_{100}}=1.38\times10^7$ cm/sec, thus exceeding the experimental values by more than 50%.

The improvement of the agreement at high temperature confirms our expectations, since the band model of Eq. (8) with $\beta=0.69$ becomes more and more adequate for higher carrier equilibrium energies.[37] In fact, at high temperatures and for fields considered here, the emission processes become less important at low temperatures, and the presence of absorption processes sharply reduces the importance of the effect on v_d of the small mass region in $\vec{k}$ space. As an example, at $E=10^4$ V/cm and $T=300$ °K absorption process are about 60% of the emission process.

Theoretical and experimental values of the anisotropic factor $(v_{d_{100}}/v_{d_{111}}-1)$ are plotted as a function of temperature in Fig. 11(a) for $E=10^3$ V/cm and Fig. 11(b) for $E=10^4$ V/cm. The anisotropy found experimentally is interpreted satisfactorily by theory over the whole range of temperatures and for different electric fields. This strongly suggests that the anisotropic factor depends basically on the warping factor η, which for the two directions $\langle 100\rangle$ and $\langle 111\rangle$ assumes the value $\eta=0.61$ and is independent of nonparabolicity effects. The anisotropic behavior shown by experiments for $v_{d_{100}}$ and $v_{d_{110}}$ has

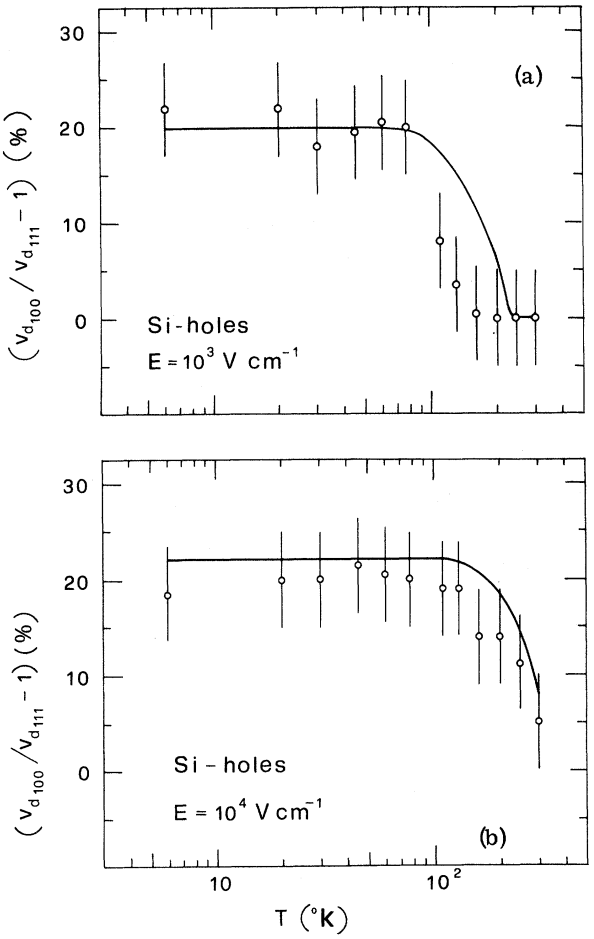

FIG. 11. (a) Anisotropic factor $(v_{d_{100}}/v_{d_{111}}-1)$ as a function of temperature in Si for an electric field $E=10^3$ V/cm. The continuous line refers to the theoretical calculations for the case $m_h/m_0=1.7$ (i.e., $\beta=0.69$). o—present data. (b) The same as in (a) for an electric field $E=10^4$ V/cm.

not been quantitatively interpreted, since the dependence of the k_{100}/k_{110} on nonparabolicity has not been incorporated in the band model used.

It should be noted that the omission of the light band in the computation at high fields should not introduce serious errors in the determinations of v_d. In the Ohmic case, a maximum underestimation of 25% was found from comparison of the single and double-band models, as previously seen in Sec. IV. A. However, the above error should be reduced at higher-field strength, since in the non-Ohmic region a depopulation of the light-hole band is expected.[38]

Energy equipartition approximation has been found to lose validity below about 77 °K, where the zero-point approximation[39] has been used. In these calculations carrier-carrier scattering was neglected and the phonon populations were assumed to be not disturbed by the presence of current. The small density of traveling carriers (10^{11}–10^{13} cm^{-3})[1] justifies the above approximation. Similar results concerning the anisotropy of the hot-hole drift velocity have been obtained for the case of Ge.[40]

ACKNOWLEDGMENTS

The authors wish to thank Dr. C. Jacoboni and Dr. M. Costato for their constructive suggestions and comments. Thanks are also due to Dr. P. Lawaetz for stimulating discussion of many aspects of the subject, and to P. Cantoni and M. Bosi for their assistance in collecting the experimental data.

APPENDIX: SCATTERING PROBABILITY FOR HOLES

Following the procedure used in Ref. 22 we evaluated the integrated scattering probability $\mathcal{P}(\vec{k}) = \int P(\vec{k}, \vec{k}')\, d\vec{k}'$ for optical- and acoustic-phonon interaction within the heavy-hole band using the energy spectrum of Eq. (8) and the scattering probability of Eqs. (1)–(4). For $G(\nu) = \frac{1}{2}$ (no overlap accounted)

$$\mathcal{P}_{op} = \frac{(D_t K)^2}{2^{1/2}\pi\hbar^2 \rho K_B \theta_{op}} (N_{op} + \tfrac{1}{2} \pm \tfrac{1}{2})(\epsilon \pm K_B \theta_{op})^{1/2} m_D^{3/2}\,, \tag{A1}$$

$$\mathcal{P}_{ac,eq} = \frac{E_1^{0^2}(K_B T)}{2^{1/2}\pi\hbar^4 \rho s^2} \epsilon^{1/2} m_D^{3/2}\,, \tag{A2}$$

$$\mathcal{P}_{ac,zp} = \frac{4E_1^{0^2}}{3\pi\hbar^4 \rho s} \epsilon m_{DD}^2 \tag{A3}$$

with

$$m_D^{3/2} = m_0^{3/2} \frac{1}{4\pi A^{3/2}(1-\beta)^{3/2}} \times \int_0^{2\pi}\int_0^{\pi} [1 - g(\vartheta, \varphi)]^{-3/2} \sin\vartheta\, d\varphi\, d\vartheta\,,$$

$$g(\vartheta, \varphi) = [b^2 + c^2(\sin^4\vartheta \cos^2\varphi \sin^2\varphi + \sin^2\vartheta \cos^2\vartheta)]^{1/2}\,, \tag{A4}$$

$$m_{DD}^2 = m_0^2 \frac{3}{2^{7/2}\pi A^2 (1-\beta)^2} \int_0^{2\pi}\int_0^{\pi} \frac{\sin\vartheta(1-\cos\vartheta)^{1/2}}{[1 - g(\vartheta, \varphi)]^2} d\varphi\, d\vartheta. \tag{A5}$$

For $G(\nu) = \frac{1}{4}(1 + 3\cos^2\nu)$ (overlap accounted)

$$\mathcal{P}_{op}^{o} = \tfrac{1}{2}\mathcal{P}_{op}\,; \quad \mathcal{P}_{ac}^{o} = \tfrac{1}{2}\mathcal{P}_{ac}\,, \tag{A6}$$

where the ± signs in Eq. (A1) refer to the absorption and emission cases and the subscripts eq and zp refer to energy equipartition and zero-point approximation, respectively. Eq. (A5) represents an approximation valid within the small-warping limit. In the present case we have estimated that the error introduced by this approximation in the evaluation of m_{DD} does not exceed 5%. Furthermore, in calculations m_D has been assumed equal to m_{DD} since both values have been found equal to 0.54 ± 0.02. It is worth noting that in the zero-point approximation the scattering probability is proportional to the energy of the carrier, while in energy equipartition it is proportional to its square root. Consequently, for hot carriers the zero-point approximation has the net effect of increasing the scattering efficiency. The superscript o in Eq. (A6) stands for the accounting for overlap.

---

*Partially supported by Consiglio Nazionale delle Ricerche, Italy.

[1] C. Canali, C. Jacoboni, F. Nava, G. Ottaviani, and A. Alberigi-Quaranta, Phys. Rev. B (to be published).
[2] C. Canali, G. Ottaviani, and A. Alberigi-Quaranta, J. Phys. Chem. Solids 32, 1707 (1971).
[3] A. Alberigi-Quaranta, C. Jacoboni, and G. Ottaviani, Riv. Nuovo Cimento 1, 445 (1971).
[4] C. B. Norris and J. F. Gibbons, IEEE Trans. Electron. Devices ED-14, 38 (1967).
[5] M. Martini, J. W. Mayer, and K. Zanio, *Advances in Solid State Science*, edited by R. Wolfe (Academic, New York, 1972), Vol. 3.
[6] W. E. Spear, J. Non-Cryst. Solids 1, 197 (1969).
[7] C. Canali, M. Costato, G. Ottaviani, and L. Reggiani, Phys. Rev. Lett. 31, 536 (1973). In this, paper there are some misprints in Eq. (3). Furthermore, in Fig. 1 the experimental electric field must be decreased by a factor of 10.
[8] R. A. Logan and A. J. Peters, J. Appl. Phys. 31, 122 (1960).
[9] G. W. Ludwig and R. L. Watters, Phys. Rev. 101, 1699 (1956).
[10] F. J. Morin, J. H. Geballe, and C. Herring, Phys. Rev. 105, 525 (1957).
[11] F. J. Morin and P. J. Maita, Phys. Rev. 96, 28 (1954).
[12] For a detailed discussion on the effect of long-range electrostatic forces, neglected here, see Ref. 13.
[13] P. Lawaetz, Phys. Rev. 183, 730 (1969).
[14] H. Ehrenreich and A. W. Overhauser, Phys. Rev. 104, 331 (1956).
[15] W. A. Harrison, Phys. Rev. 104, 1281 (1956).
[16] H. Ehrenreich and A. W. Overhauser, Phys. Rev. 104,

649 (1956).
[17]G. L. Bir and G. E. Pikus, Fiz. Tverd. Tela 2, 2287 (1960) [Sov. Phys. – Solid State 2, 2039 (1961)].
[18]J. Bardeen and W. Shockley, Phys. Rev. 80, 72 (1950).
[19]G. D. Whitfield, Phys. Rev. Lett. 2, 204 (1959); and Phys. Rev. 121, 720 (1961).
[20]M. Tiersten, J. Phys. Chem. Solids 25, 1151 (1964).
[21]J. D. Wiley, Phys. Rev. 4, 2485 (1971).
[22]M. Costato and L. Reggiani, Phys. Status Solidi B 58, 461 (1973), and B 58, 47 (1973).
[23]Owing to symmetry there are no *a priori* arguments for the angular dependence of the hole optical-phonon matrix element (Ref. 24), consequently the present choice has to be intended as a working assumption.
[24]P. Lawaetz, Phys. Rev. 174, 867 (1968), and private communication.
[25]J. J. Hall, Phys. Rev. 161, 756 (1967).
[26]B. N. Brockhouse, Phys. Rev. Lett. 2, 256 (1959).
[27]M. Costato and S. Scavo, Intituto Nazionale di Fisica Nucleare INFN/FM 68/4 (1968) (unpublished).
[28]I. Balslev and P. Lawaetz, Phys. Lett. 19, 6 (1965).
[29]P. Lawaetz, Phys. Rev. B 4, 3460 (1971).
[30]G. Dresselhaus, A. F. Kip, and C. Kittel, Phys. Rev. 131, 2442 (1963).
[31]E. O. Kane, J. Phys. Chem. Solids 1, 82 (1956).
[32]H. Krömer, in *Progress in Semiconductors*, edited by A. F. Gibson (Heywood, London, 1960), Vol. 4, p. 1ff.
[33]W. Fawcett, A. D. Boardman, and S. Swain, J. Phys. Chem. Solids 31, 1963 (1970).
[34]Equation (6) introduces a discontinuity in τ at ϵ_0 and ϵ_1, however, this fact does not create difficulties concerning the final mobility.
[35]M. Costato, G. Gagliani, C. Jacoboni, and L. Reggiani, J. Phys. Chem. Solids 35, 1605 (1974).
[36]M. Asche and J. von Borzeszkowski, Phys. Status Solidi B 37, 433 (1970).
[37]L. Reggiani, G. Majni, and R. Minder, Solid State Commun. 16, 151 (1975).
[38]W. E. Pinson and R. Bray, Phys. Rev. 136, 1449 (1964).
[39]M. Costato and L. Reggiani, Nuovo Cimento Lett. 4, 1179 (1970).
[40]L. Reggiani, C. Canali, F. Nava, G. Ottaviani, and P. Lawaetz, in *Proceedings of the Twelfth International Conference on the Physics of Semiconductors*, edited by M. H. Pilkuhn (Teubner, Stuttgart, 1974), p. 819.